Research Square

Preprints are preliminary reports that have not undergone peer review.
They should not be considered conclusive, used to inform clinical practice,
or referenced by the media as validated information.

Intravital lung microscopy unveils T cell dynamics in mouse tuberculosis lesions

Léa Fromont
Institut de Pharmacologie et de Biologie Structurale (IPBS), Université de Toulouse, CNRS, UPS, Toulouse, France

Aizat Iman Abdul Hamid
Institut de Pharmacologie et de Biologie Structurale (IPBS), Université de Toulouse, CNRS, UPS, Toulouse, France

Elisabeth Bellard
Institut de Pharmacologie et de Biologie Structurale (IPBS), Université de Toulouse, CNRS, UPS, Toulouse, France

Zachary P. Howard
Division of Experimental Medicine, Department of Medicine, University of California San Francisco, San Francisco, CA, USA

Sarah Monard
Institut de Pharmacologie et de Biologie Structurale (IPBS), Université de Toulouse, CNRS, UPS, Toulouse, France

Jean-Philippe Girard
Institut de Pharmacologie et de Biologie Structurale (IPBS), Université de Toulouse, CNRS, UPS, Toulouse, France

Etienne Meunier
Institut de Pharmacologie et de Biologie Structurale (IPBS), Université de Toulouse, CNRS, UPS, Toulouse, France

Denis Hudrisier
Institut de Pharmacologie et de Biologie Structurale (IPBS), Université de Toulouse, CNRS, UPS, Toulouse, France

Olivier Neyrolles
Institut de Pharmacologie et de Biologie Structurale (IPBS), Université de Toulouse, CNRS, UPS, Toulouse, France

Serge Mazères
Institut de Pharmacologie et de Biologie Structurale (IPBS), Université de Toulouse, CNRS, UPS, Toulouse, France

Joël D. Ernst
Division of Experimental Medicine, Department of Medicine, University of California San Francisco, San Francisco, CA, USA.

Emma Lefrançais

emma.lefrancais@ipbs.fr

Institut de Pharmacologie et de Biologie Structurale (IPBS), Université de Toulouse, CNRS, UPS, Toulouse, France https://orcid.org/0000-0003-0489-9298

Research Article

Keywords:

Posted Date: December 3rd, 2025

DOI: https://doi.org/10.21203/rs.3.rs-8259909/v1

License: This work is licensed under a Creative Commons Attribution 4.0 International License. Read Full License

Additional Declarations: The authors declare no competing interests.

Abstract

Protective immunity to *Mycobacterium tuberculosis* (*Mtb*) depends on the ability of T cells to access and engage infected cells within lung lesions, yet these spatiotemporal interactions remain poorly defined. Direct intravital imaging of *Mtb*-infected lungs has historically been limited by biosafety and technical constraints, preventing real-time visualization of immune dynamics *in situ*. Here, we present LiveLung-TB, a biosafety level 3–compatible lung intravital imaging platform that enables high-resolution imaging of immune cell behavior in *Mtb*-infected lungs. Using this approach, we demonstrate that although most $CD4^+$ T cells infiltrate the infected parenchyma, only a small fraction forms transient (~11%) or stable (~5%) contacts with infected macrophages. Strikingly, the majority remain immobilized or display intermittent migration within uninfected, collagen-rich regions or at the periphery of macrophage clusters, independently of antigen recognition. These findings uncover previously unrecognized physical and microenvironmental barriers that restrict T cell motility and limit productive effector engagement. LiveLung-TB thus provides a powerful framework to elucidate and ultimately overcome tissue-imposed constraints on immune efficacy in tuberculosis and other pulmonary infections.

Introduction

Mycobacterium tuberculosis (*Mtb*), the causative agent of tuberculosis (TB), remains the leading cause of death from a single infectious agent worldwide (*Global Tuberculosis Report 2025* 2025). Despite decades of research, our understanding of the mechanisms that limit bacterial clearance in the lungs, and our ability to overcome them with improved vaccines or therapeutics, remains incomplete, and antibiotic-resistant strains continue to emerge. T cell–mediated immunity, especially via $CD4^+$ lymphocytes, is central to host defence against *Mtb*, yet protective efficacy is often incomplete, allowing long-term survival of the pathogen (Jasenosky et al. 2015; Flynn et Chan 2022; Lefrançais et al. 2025). While T cell activation and differentiation in lymphoid organs are well characterized, the mechanisms that govern their migration, positioning, and interactions with infected cells in the lung remain poorly understood. Effective immunity requires that effector T cells reach infected sites and establish stable contacts with *Mtb*-infected macrophages (Srivastava et Ernst 2013), yet histological analyses reveal a striking spatial segregation: infected macrophages are concentrated in granuloma cores, whereas T cells localize predominantly at the periphery (Cohen et al. 2022; Kauffman et al. 2018; Gideon et al. 2022; McCaffrey et al. 2022). The dynamic processes underlying this spatial segregation in the lung have remained entirely uncharacterized, largely because imaging a living, ventilated lung under BSL-3 containment has, until now, been technically impossible. Intravital microscopy has revolutionized our understanding of T cell behavior in tumors and other infectious settings by enabling real-time visualization of cell recruitment, migration, and interactions within intact tissues (Hor et Germain 2022; Pittet et al. 2018; Sumen et al. 2004; Boulch et al. 2019). Yet this approach has never been applied to *Mtb*-infected lungs, where continuous respiratory motion, the need to preserve physiological function, and stringent biosafety constraints have prevented high-resolution imaging (Looney et Headley 2020). In hepatic BCG granulomas, intravital microscopy has revealed that T cells are rapidly recruited to and retained within granuloma structures, and that their migration is constrained by a macrophage-defined

boundary (Egen et al. 2008). Within these structures, dynamic tracking of antigen-specific T cells showed that they remain highly motile and rarely arrest on antigen-presenting cells (Egen et al. 2011), suggesting that effective cognate recognition may be limited. In pulmonary TB, real-time dynamics of T cell–macrophage interactions have not been directly observed, leaving open questions about whether peripheral accumulation reflects insufficient antigen presentation, microenvironmental constraints, or both. Overcoming these obstacles is essential to uncover the mechanisms that constrain T cell access to infected macrophages and to understand why T cell responses often fail to clear *Mtb* (Lefrançais et al. 2025). Here, we developed a BSL-3–compatible intravital lung microscopy platform that enables high-resolution, real-time imaging of immune–pathogen interactions in *Mtb*-infected lungs. Using this platform, we generate the first *in vivo*, real-time dynamic map of T lymphocytes within TB lesions, uncovering intermittent migration patterns and a high frequency of arrests occurring away from infected cells. We further show how vascular architecture, extracellular matrix organization, and macrophage cluster collectively shape $CD4^+$ T cell positioning, motility, and engagement with infected macrophages. These findings provide new mechanistic insight into why T cells accumulate at a distance from infected cells and offer a framework for understanding immune evasion by *Mtb* in the lung.

Results

LiveLung-TB: a BSL-3 intravital microscopy platform for real-time imaging of TB lesions

To visualize immune dynamics in *Mtb*–infected lungs in real time, we developed LiveLung-TB, a biosafety level 3 compatible intravital lung microscopy system. The platform integrates a dedicated surgical setup (Fig. 1a-b), a TB lesion–adapted thoracic window (Fig. 1c), and procedures within a BSL-3 facility, equipped with a two-photon microscope (Barlerin et al. 2017) (**Extended Data** Fig. 1). Mice are prepared under a biosafety hood, transferred securely to the microscope isolator, and mechanically ventilated throughout imaging, enabling high-resolution, long-term intravital visualization under full containment (**Extended Data** Fig. 1). The system features a custom surgical plate for safe transport and manipulation of anesthetized animals (Fig. 1a) and an adapted imaging window that stabilizes the left lung under gentle suction for high-resolution visualization of subpleural TB lesions. The TB lesion–specific thoracic window was derived from previously described intercostal lung IVM windows (Headley et al. 2016; Looney et al. 2011), with key modifications including a steeper angle to optimize objective displacement and a flattened base to ensure stable placement over visible TB lesions (Fig. 1c, 1d). We combined this imaging platform with optimized reporter systems to visualize key cellular components (Fig. 2a-b). Fluorescent *Mtb* bacilli expressing mTurquoise enabled visualization of individual bacteria and small clusters (Fig. 2c-d). In parallel, infected macrophages were imaged in Siglec1-Cre × mTmG mice, in which macrophage membranes fluoresce green (GFP) and lung structural cells fluoresce red (mTomato) (Fig. 2c-d). Lesions were readily identifiable, characterized by vascular remodeling, collapsed alveoli, macrophage aggregates, clusters of infected macrophages harboring mTurquoise-labeled bacteria (Fig. 2d **and Extended Data** Fig. 2), and multinucleated giant cells (**Extended Data** Fig. 3a). In

contrast, healthy lungs displayed preserved alveolar architecture, with large alveolar spaces, thin alveolar walls lined by capillaries, and sparse macrophages (**Extended Data** Fig. 3b). To quantify lesion size and heterogeneity accessible by lung intravital microscopy, we measured 53 subpleural lesions using 2D maximum intensity projections. Lesions were defined by macrophage clustering, intracellular bacteria, and clear boundaries formed by local tissue remodeling (**Extended Data** Fig. 2). Lesion size were heterogenous, equivalent diameters ranging from 179 to 1022 µm (mean 516 µm, SD 203 µm) (**Extended Data** Fig. 3c). 3D-cleared whole-lobe lung imaging combined with lesion segmentation (Fig. 3a–b) revealed marked lesion heterogeneity, with diameter ranging from 2 to 2,114 µm (mean 646 µm, SD 453), and confirmed that 3D mosaic acquired with the thoracic window (volume of 1134 × 756 × 100 µm) can cover most of lesions in xy and approximately half in z (Fig. 3c–d). Segmentation revealed complex, often mushroom-shaped lesion architecture connected to airways, predominantly expanding in the XY plane, making subpleural lesions readily accessible for live imaging (Fig. 3b-d). Together, these results establish LiveLung-TB as an efficient and adapted technique for studying immune–pathogen interactions within intact *Mtb*-infected lungs in real time.

Vascular remodeling and perfusion in TB lesions

Vascular remodeling is a hallmark of chronic inflammatory lesions, including those caused by *Mtb*. In TB granulomas, persistent inflammation and hypoxic stress trigger angiogenic responses, leading to dense, tortuous, and disorganized vascular networks (Datta et al. 2015; Oehlers et al. 2015; Wells et al. 2021). Despite this increased vessel density, the functionality of the granuloma vasculature and the extent of tissue oxygenation remain unclear. While some studies describe hypoxic or necrotic cores, others suggest that subsets of granulomas maintain limited perfusion sufficient to sustain immune activity. To directly assess vascular architecture and function *in vivo*, we performed intravital microscopy of *Mtb*-infected lungs, using mTomato labeling of stromal membranes to visualize vessels and surrounding parenchyma (Fig. 2d, **Extended Data** Fig. 2). This analysis revealed pronounced vascular remodeling within lesions, with marked increases in vessel density and tortuosity. Perfusion and permeability assays using fluorescent dextran and Evans Blue (**Extended Data** Fig. 4a,b and **Supplementary Video 1**) showed that, although granulomas remain perfused, they exhibit extensive vascular leakage into alveolar spaces compared with adjacent healthy regions. Collectively, these findings indicate that TB lesions contain a highly remodeled and permeable vasculature, potentially influencing immune cell trafficking and the local inflammatory environment.

CD4⁺ T cells infiltrate TB lesions and preferentially localize around infected macrophage clusters

To characterize CD4⁺ T cell dynamics in *Mtb*-infected lungs, we performed adoptive transfer of Th1-polarized, Deep Red–labeled *Mtb*-antigen specific (C7, recognizing the ESAT-6 antigen) CD4⁺ T cells, isolated from the spleens of donor mice, into chronically infected recipients. Between 5×10^6 and 5×10^7 cells were transferred intravenously, and their migration was tracked 24 hours later by lung intravital

microscopy (LIVM) (Fig. 4a and **Supplementary Video 2**). A custom tracking pipeline was developed to quantify T cell motility, including track length, displacement, velocity, straightness, and behavioral parameters such as localization, directionality, and cell–cell interactions (**Extended Data** Fig. 5a). We tracked 911 CD4⁺ T cells for 30 to 60 minutes in three independently infected mice. We examined CD4⁺ T cells spatial distribution relative to granulomatous lesions and clusters of infected macrophages, as previously defined (**Extended Data** Fig. 2). Mapping of T cell tracks revealed that 88.8 ± 5.8% of transferred CD4⁺ T cells infiltrated TB lesions and were predominantly concentrated around clusters of infected macrophages (Fig. 4b-d), highlighting a targeted localization of CD4⁺ T cells within granulomatous microenvironments.

Lung intravital imaging reveals distinct CD4⁺ T cell migratory states and predominant parenchymal arrest during M. tuberculosis infection

We further analysed their migratory behaviour, revealing three distinct migratory profiles in *Mtb*-infected lungs: rapidly mobile intravascular cells, mobile extravascular cells migrating within the parenchyma, and arrested extravascular cells (Fig. 5a-c, **Supplementary Video 3**). These migratory profiles were confirmed by unsupervised clustering of discriminative motility parameters (**Extended Data** Fig. 5b) and mean square displacement (MSD) analysis (**Extended Data** Fig. 5c-d). Intravascular cells, representing 8.8 ± 2.5% of all tracks (Fig. 5d), displayed the highest average and maximum velocities, greater displacements, and more linear directed trajectories, reflected by elevated straightness and α coefficients (Fig. 5f-i, **Extended Data** Fig. 5d), but were tracked over shorter time intervals (**Extended Data** Fig. 5b**)**. The majority of C7 T cells (91.2 ± 2.5%) were extravascular (Fig. 5d) and could be subdivided into two main subsets: arrested cells (57.5 ± 10.1%) and mobile cells (42.5 ± 10.1%) (Fig. 5e). Extravascular T cells exhibited intermittent motility, alternating between brief movements and transient pauses, as reflected by their instantaneous velocity and arrest coefficient, the latter defined as the percentage of time moving below 2 μm/min (Fig. 5j-m). Together, these data delineate three distinct CD4⁺ T cell migratory behaviors within *Mtb*-infected lungs, reflecting the spatial and kinetic diversity of T cell behavior in granulomatous tissue. While T cell intermittent migration has been previously observed in pulmonary environments (Mrass et al. 2017), the large fraction of extravascular T cells exhibiting sustained arrest was unexpected. This contrasts with hepatic granulomas induced by *Mycobacterium bovis* BCG, where mycobacteria-specific T cells remain predominantly motile and form few stable contacts with antigen-presenting cells (Egen et al. 2011), suggesting that the pulmonary microenvironment imposes unique constraints on T cell dynamics during TB.

CD4⁺ T cells show only rare and transient interactions with infected macrophages

To explore the basis of the prolonged arrest and intermittent migration of CD4⁺ T cells in TB lesions, we examined their interactions with infected macrophages (**Supplementary Video 4**). While stable contacts with antigen-presenting cells are typically driven by TCR-mediated antigen recognition, only a minority of

CD4⁺ T cells engaged directly with infected macrophages, (16.9 ± 10.5% of tracked cells) (Fig. 6a). Among these, only 36.6 ± 10.7% underwent stable arrest (Fig. 6b, 6c), corresponding to just 5.4 ± 1.4% of the total extravascular T cell population (Fig. 6d). The remaining mobile CD4⁺ T cells (63.4%) made only transient contacts with infected cells (Fig. 6b, 6c), characterized by short-lived arrests (7.4 ± 8.5 min; range 1.8–31.0 min) (Fig. 6e-h). These arrest durations are consistent with initial scanning interactions, exploratory and low-affinity, and therefore insufficient for activation (Celli et al. 2007), and were comparable to the brief pauses observed during intermittent migration of cells that did not contact infected cells (Fig. 6f-h). These observations indicate that CD4⁺ T cell encounters with infected macrophages are rare, and when they do occur, they are predominantly brief, low-affinity interactions.

CD4⁺ T cell arrest in Mtb granulomas occurs independently of antigen recognition

Given that interactions with infected cells were rare and unstable, we next sought to identify the mechanisms underlying the predominant parenchymal arrest of CD4⁺ T cells (Fig. 5e). To directly test whether antigen recognition influences T cell arrest within pulmonary granulomas, we compared the migratory behavior of *Mtb*-specific (C7, recognizing the ESAT-6 antigen) and non-specific (OT-II, recognizing the OVA peptide) CD4⁺ T cells using lung intravital microscopy (Fig. 7a, **Supplementary Video 5**). Analysis of motility parameters, including the proportion of arrested cells, arrest coefficient, average speed, and displacement, revealed no significant differences between C7 and OT-II T cells (Fig. 7b-e). These results indicate that T cell arrest and migratory behavior within *Mtb*-infected lungs are not dependent on antigen recognition, suggesting that factors other than TCR engagement, such as the local microenvironment, cytokine gradients, or extracellular matrix organization, may predominantly regulate T cell dynamics within granulomas.

CD4⁺ T cell interactions with collagen fibers and macrophage clusters in TB lesions

To understand why CD4⁺ T cell encounters with infected macrophages are rare, we analyzed their spatial distribution relative to infected cells and examined their interactions with surrounding cellular and structural elements. Most CD4⁺ T cells were positioned 20–40 μm away from infected macrophages, and, unexpectedly, arrested cells were located even farther from infected cells than mobile ones (32 ± 7 μm vs. 23 ± 7 μm) (Fig. 8a-b). Interaction analysis revealed three main elements associated with T cell arrest at a distance from infected macrophages: uninfected macrophages (**Supplementary Video 6)**, collagen fibers (**Supplementary Video 7)**, and other non-identified structures, with no difference in their distance to infected cells (Fig. 8b–c). A substantial proportion of CD4⁺ T cells (32.1 ± 5.3%) interacted with uninfected macrophages (Fig. 8e, **Supplementary Video 6**), typically at the periphery of macrophage clusters (**Extended** Fig. 6a), whereas bacteria accumulated in the center. Among T cells contacting uninfected macrophages, 60.1 ± 6.6% were arrested (Fig. 8f–h). Second harmonic generation (SHG) imaging showed extensive collagen deposition encasing macrophage aggregates within TB lesions (**Extended** Fig. 6b). Intravital microscopy revealed that 39.1 ± 4.9% of CD4⁺ T cells were closely

associated with collagen fibers, either remaining arrested (54.5 ± 10.2%) or migrating along these structures (Fig. 8i–l, **Supplementary Video 7**), indicating that collagen-rich regions provide both structural scaffolds and guidance cues for T cell movement. Similar ECM-guided migration has been documented in inflamed dermis, brain, and tumors, where fiber orientation and density channel T cell trajectories and constrain access to target cells. Importantly, $CD4^+$ mobile T cells did not show preferential or prolonged arrest on uninfected macrophages, collagen fibers, or other non-identified structures (**Extended** Fig. 6e–g), and their distance from infected cells as well as their intermittent migration pattern were independent of the interacting partner (Fig. 8c). Directional analysis further demonstrated that 70% of mobile extravascular T cells migrated along the periphery of lesions rather than toward infected macrophages (Fig. 8d). Together, these findings indicate that collagen fibers and the organization of macrophage clusters strongly shape $CD4^+$ T cell motility and positioning, thereby limiting productive contacts with infected cells and potentially contributing to the long-term survival of *Mtb* within granulomatous tissue.

Discussion

In this study, we present LiveLung-TB, the first platform enabling real-time visualization of T cell migration within *Mtb*-infected lung lesions. This technique provides a detailed view of $CD4^+$ T cell dynamics, revealing unique migration behaviors. Our results reveal that lymphocytes rarely establish stable contacts with infected macrophages and preferentially localize to the periphery of macrophage clusters, where they arrest or migrate along non infected macrophages and collagen fibers. By combining multiphoton intravital imaging with fluorescent labeling, we directly observed how tissue architecture, vascular remodeling, cell aggregates and ECM composition shape immune cell behavior *in situ*.

Granulomas frequently exhibit poorly perfused and structurally altered vasculature (Wells et al. 2021; Datta et al. 2015; Oehlers et al. 2015), which limits T cell extravasation and restricts their access to lesion cores. Such vascular remodeling and perfusion defects likely represent major drivers of immune cell exclusion, as similarly reported in tumors and other chronic inflammatory settings where physical access can be as limiting as effector function. Lung intravital imaging is essential to dissect these dynamics, and our observations in the C57BL/6 mouse model reveal that lymphocytes do infiltrate TB lesions, although the extensive vascular remodeling and increased leakiness may shape their migratory behavior within lesions.

We find that only a minority of lymphocytes engage infected macrophages, with ~ 11% forming transient contacts and only ~ 5% establishing stable interactions. These low frequencies point to two sequential limitations: restricted physical access to infected cells, and suboptimal activation even when contact occurs. Stable T cell–macrophage interactions depend on antigen-specific TCR engagement (Moreau et al. 2015). Yet, consistent with observations in BCG-induced hepatic granulomas (Egen et al. 2011), most $CD4^+$ T cells that reach infected macrophages remain highly mobile and rarely form sustained contacts, suggesting low-affinity antigen recognition or insufficient signaling. Notably, in both human lung biopsies and macaque infection models, *Mtb*-specific $CD4^+$ T cells also infrequently contact infected

macrophages despite evidence of activation (Kauffman et al. 2018), underscoring the combined impact of anatomical constraints and functional limitations.

Strikingly, the majority of parenchymal lymphocytes remain immobilized or display intermittent migration at a distance of 10–20 μm from infected macrophages, typically along collagen fibers or at the periphery of macrophage aggregates, and this behavior occurs independently of antigen recognition. Our observation that T cells migrate within the boundaries of macrophage clusters is reminiscent of T cell behavior in BCG-induced granulomas, where their movement is also constrained by macrophage-defined borders (Egen et al. 2008). Granulomas and macrophage cluster are encased in dense fibrotic networks composed of collagen, fibronectin, laminin (Kauffman et al. 2018; Sawyer et al. 2023) and other ECM components, and ECM architecture is known to strongly influence T cell motility. Our observation that $CD4^+$ T cells frequently arrest and migrate along collagen fibers mirrors ECM-guided migration described in lymph nodes, lung tissue, tumors, and other inflamed environments, where fiber density and orientation shape T cell trajectories (Overstreet et al. 2013; Salmon et al. 2012; Wilson et al. 2009; You et al. 2021; Mrass et al. 2017). Stromal networks, such as fibroblastic reticular cells (FRC), also play a central role in directing lymphocyte migration in lymph nodes (Bajénoff et al. 2006) and peripheral tissues, including lung tumors (Onder et al. 2025), where T cells move along CCL19-expressing FRC-defined tracks. These parallels raise the possibility that similar stromal or ECM-derived guidance cues operate within lung TB granulomas, simultaneously directing T cell movement and restricting their access to infected targets.

Surprisingly, OT-II cells (non–*Mtb* specific) exhibit similar migratory behaviors, indicating the involvement of antigen-independent mechanisms that remain to be identified. T cell positioning can be shaped by recent activation or memory status independently of cognate antigen recognition (Topham et al. 2001). Integrins such as VLA-1 (α1β1), which binds collagen and mediates the retention of protective memory T cells in non-lymphoid tissues including the lung (Ray et al. 2004), exemplify how the ECM not only imposes physical constraints but may actively organize T cell retention and spatial distribution within granulomas. Additional adhesion pathways (LFA-1; CD2/LFA-3), chemokine gradients, glycosaminoglycans, cytokines and stromal inhibitory signals can similarly promote transient arrest or reduced motility (Gunzer et al. 2000; Kerdidani et al. 2022). Extracellular ATP sensed by P2RX7 on $CD4^+$ T cells enhances their tissue accumulation by inducing CXCR3 expression (Santiago-Carvalho et al. 2023), and potent chemokine cues can even override MHC–peptide-driven positioning (Bromley et al. 2000). Moreover, homeostatic cytokines help maintain tissue-resident T cell populations despite dynamic desensitization to antigenic stimulation (Boldajipour et al. 2016). Thus, LiveLung-TB will uniquely enable dissection of these physical and molecular constraints in real time, providing a platform to evaluate how chemokines, adhesion molecules, and antigen availability influence T cell positioning and effector function.

Limitations include the use of C57BL/6 mice, which are relatively resistant to *Mtb* and do not form fully structured granulomas. Imaging more susceptible models, such as SP140-deficient mice (Ji et al. 2021), will be interesting improving translational relevance. Adoptively transferred T cells were analyzed shortly

after transfer (24 h); longer residence times may influence motility and functional adaptation (Boldajipour et al. 2016; You et al. 2021). Longitudinal imaging could clarify how activation or exhaustion states affect migration and arrest. The molecular mechanisms mediating T cell–ECM and T cell–macrophage interactions remain to be defined; identifying the relevant receptors and integrins, and perturbing them, will clarify whether ECM serves primarily as a scaffold or barrier and whether modulating these interactions can improve access to infected macrophages.

In conclusion, LiveLung-TB provides a dynamic and mechanistic view of immune cell behavior in *Mtb*-infected lungs. If physical and molecular barriers limit access to infected macrophages, vaccines or immunotherapies that increase T cell numbers or activation may be insufficient. Strategies such as vascular normalization, ECM remodeling, or chemokine modulation could enhance bacterial clearance. This platform offers a roadmap to dissect the spatial and temporal determinants of T cell access to infected macrophages and to test interventions aimed at enhancing immunity and improving outcomes in TB.

Material et Methods

Mice

Male and female mice aged 6-12 weeks were used throughout the study. C7TCR-Tg Nur77-GFP mice were kindly provided by Dr. Ernst Joel (UCSF, USA) and. Siglec1-mTmG were obtained by crossing Siglec1-cre with Rosa26-mTmG mice (IPBS, France). OVA-specific $CD4^+$ TCR Tg (OTII; Charles River, France) mouse were purchased. All mice were bred at the Institute of Pharmacology and Structural Biology (IPBS) UMR 5089 (agreement F31555005) and procedures complied with French regulations and were approved by the Ministry of Higher Education and Research (APAFIS agreements 47848 and 34716).

Bacteria

Fluorescent derivatives of the wild-type M. tuberculosis Erdman strain were constructed by transformation of this strain with pGMCS-P1-mTurquoise. Plasmids pGMCS-P1-mTurquoise are integrative vectors in mycobacteria that confer resistance to streptomycin and constitutively express mTurquoise fluorescent reporter. They were constructed by Gateway cloning, as described previously (Ariyachaokun et al. 2020). *M. tuberculosis* Erdman and its fluorescent mTurquoise transformants were cultured in suspension in Middlebrook 7H9 medium (BD) supplemented with 10% albumin-dextrose-catalase (ADC, BD) and 0.05% Tyloxapol (Sigma). For infection, exponentially growing cultures were centrifuged at 2,301 × *g*, resuspended in phosphate-buffered saline (PBS; Gibco), and de-aggregated by vortexing with glass beads. Remaining clumps were removed by a low-speed spin (120 × *g*). Bacterial concentration was estimated by measuring the optical density at 600 nm (OD_{600}), and the suspensions were adjusted in PBS for *in vivo* infection.

Mouse infection

Mice were exposed to *M. tuberculosis* Erdman in an inhalation tower (Buxco Inhalation Exposure System, DSI) calibrated to deliver 100 colony-forming units (CFUs) to the lungs per mouse.

CD4 lymphocyte isolation and polarization and adoptive transfer

Mice were anesthetized with isoflurane and euthanized by cervical dislocation. Naïve $CD4^+$ T cells were magnetically isolated from spleen cell suspensions of C7TCR-Tg mouse or OTII mice using anti-CD4 microbeads (L3T4) (Miltenyi Biotec) according to the manufacturer's instructions. $CD4^+$ T cells were cultured in the presence of Th1 skewing cytokines: mouse IL-12p70 (10 ng/ml), mouse IL-2 (20 ng/ml), CD3 (5µg/ml) and CD28 (1µg/ml). Cells were cultured at 37°C with 5% CO2. On days 3 and 5 of culture, cells were split 1:3 with fresh media containing IL-12p70 and IL-2. Cells were washed with PBS and counted on day 7 of culture before use for *in vivo* assays. On day 7 of culture, polarized Th1 CD4 lymphocytes were counted and labeled before injection. They were either labeled with CellTracker™ Deep Red or Orange (Invitrogen™) according to the manufacturer's instructions. Cells were counted and adjusted at $1x10^7$ in PBS. The mice were placed in an induction chamber and briefly anesthetized by isoflurane, 100–150 µL of the cell suspension were injected into the retro-orbital sinus using a U100 insulin syringe (BD micro-fine 0.3 mL, 30 gauge needle), 24 hours before lung intravital microscopy.

TB lesion adapted thoracic window production and assembly

The TB lesion–adapted thoracic window was modified in Blender, based on previously described intercostal lung IVM windows (Headley et al. 2016). Modifications included an increased angle to optimize objective xy movement and a flat base to facilitate stable positioning over TB lesions. Windows were 3D-printed in high-detail stainless steel (Sculpteo). An 8-mm round coverslip (Cat# 64-0701, Thomas Scientific) was inserted and sealed overnight using nail lacquer applied along the outer edge of the coverslip.

Lung intravital surgery platform construction and assembly

The platform was engineered to maintain an anesthetized, mechanically ventilated mouse throughout three consecutive phases: (i) mouse tracheotomy, mechanical ventilation, and surgical placement of the lung optical window within a microbiological safety cabinet (MSC) using a dedicated mechanical holder; (ii) transfer of the ventilated mouse from the MSC to the intravital microscopy isolator; and (iii) stable immobilization and accurate positioning of the lung beneath the microscope objective throughout image acquisition, along with connection to gas anesthesia and controlled lung aspiration onto the imaging window. The base structure consists of a PVC plate fitted with carrying handles. One section accommodates the mouse and includes an integrated support to position and secure the optical window. The mechanical ventilator and its battery are mounted on the opposite end of the platform, while ventilator tubing and pathogen-protection filters are organized via custom 3D-printed polylactic acid (PLA) holders. Additional accessories, including racks for Eppendorf tubes and holders for surgical instruments, were also 3D-printed.

Multiphoton lung intravital imaging in BSL3

Multiphoton lung intravital microscopy was performed using a BSL-3 isolated microscope (Barlerin et al., 2017). Surgical preparation was adapted from established lung IVM protocols (Headley et al., 2016; Looney et al., 2011) and carried out inside a biosafety cabinet using the dedicated surgery platform. Mice were anesthetized with ketamine/xylazine (105/3 mg/kg, i.p.) and received s.c. injections of buprenorphine (0.1 mg/kg) and Ringer Lactate (10 mL/kg). After shaving the left flank, mice were positioned supine on a heating pad mounted on the inclined (45°) surgical platform. A tracheotomy was performed and a small tracheal cannula connected to a MiniVent ventilator (Harvard Apparatus) was inserted and secured. Ventilation parameters were set to a tidal volume of 10 µL compressed air (21% O_2) per gram of body weight, a respiratory rate of 130–140 breaths per minute, and a PEEP of 2–3 cm H_2O. Mice were then placed in right lateral decubitus, and a small skin and fascia incision was made in the left flank to expose the rib cage. Two ribs were transected at each extremity and removed to create an opening adapted to the size and position of visible TB lesions, which were apparent through the intercostal muscle at this infection stage. The surgical platform was transferred from the biosafety cabinet to the microscope isolator using a sealed transfer isolator, ensuring continuous containment. Inside the microscope isolator, temperature was maintained at 30°C and anesthesia was continued with 1% isoflurane. A modified lung window was positioned over a visible lesion and lowered using optical posts and a 90° angle clamp (Thorlabs) to just above the lung surface. Gentle suction (20–25 mmHg; Dexter Medical, 0–250 mbar) was applied to stabilize the lung against the coverslip (Fig. 1d).

In Vivo vascular staining

In some experiment, Dextran, Dextran FITC 40,000 MW (250 µg, D1844 Invitrogen) or Evans Blue (100 µL of 1% wt/vol solution in PBS) were injected i.v. before imaging to visualize vasculature and its permeability.

Lung intravital acquisition

Imaging was performed on an upright TriMScope II multiphoton microscope (LaVision Biotec/Miltenyi Biotec) equipped with a 20×/1.0 NA water-immersion objective and four NDD detectors, and a Chameleon Ultra II Ti:Sapphire femtosecond laser was the excitation source (Coherent Inc.) tuned to 870 nm (Deep Red–labeled $CD4^+$ T cells only) or 855 nm (Deep Red + CTO). Emission signals from collagen/mTurquoise, GFP, Tomato/CTO, and Deep Red were collected in four separate channels using 450/50, 525/50, 595/40, and LP650 filters, respectively. Four-color image stacks were acquired at 1.4 frames/s for 405 × 405 µm fields at 512 × 512 pixels, or at for 393 × 393 µm fields at 1,024 × 1,024 pixels.

Image analysis and lymphocyte tracking

Three-dimensional time-lapse sequences (30 min to 2 h) were acquired to analyze T cell dynamics and processed using ImageJ (NIH) and Imaris 9.3.1 (Bitplane). Large xyzt mosaic movies were assembled

with the stitching plugin in Fiji/ImageJ (https://imagej.net/plugins/image-stitching), and lesion characteristics, including number, diameter, and surface area, were measured directly from the movies. For lymphocyte tracking, z-stacks were reduced using maximum intensity projection, and individual T cell trajectories (~300 cells per video) were manually tracked using the TrackMate plugin in Fiji/ImageJ (https://imagej.net/plugins/trackmate), as variable cell shape, contrast, and intensity precluded reliable automatic tracking. Three videos were analysed, each from a different infected mouse, tracking a total of 911 $CD4^+$ T cells, with an average of 300 cells per video (169, 282, and 460). Trajectory data were analyzed using in-house Python scripts to generate quantitative parameters, graphs, and tracking maps. Cluster analysis of cellular behaviors was performed using the UMAP Python package, which reduces dimensionality and identifies distinct functional groups. This approach provides a comprehensive quantitative mapping of T cell behaviors during *M. tuberculosis* infection.

Behaviour parameters definition

For each tracked T cell, the following parameters were analysed:

- Track metrics: track length (the total length of displacement within the track), displacement (the distance between the first and last lymphocyte positions), straightness (the dimensionless index ranges from 0 to 1 and quantifies the linearity of a track).
- Speed metrics: instantaneous speed, average and maximal average speed.
- Pausing behavior: arrest coefficient, defined as the percentage of time a cell's instantaneous speed was <2 μm/min; number of arrests per track, representing how many times the cell slowed below 2 μm/min; and mean arrest duration, calculated as the average length of these pauses.
- Vascular localization: intravascular (IV) versus extravascular (EV) localization was determined using lung vessel visualization (mTomato)
- Distance to infected macrophage was calculated from lymphocyte membrane to membrane of closest infected macrophage
- Mean Square Displacement (MSD) quantifies the average area covered by a lymphocyte as it moves through space over time
- Alpha (α) coefficient describes the scaling behavior of MSD over time and is obtained by fitting MSD(t) to a power-law model: an α value of $\alpha \approx 1$ indicates random (diffusive) motion, $\alpha < 1$ indicates subdiffusive or confined movement, $\alpha > 1$ indicates superdiffusive or directed motion.

All trajectory maps, tracking visualizations, and parameter calculations were generated using in-house Python scripts. Dimensionality reduction and clustering of cellular behaviors using UMAP allowed identification of distinct functional groups within the dataset.

Lung tissue clearing and 3D multiphoton microscopy

Mtb –infected lungs were fixed overnight at 4 °C in periodate–lysine–paraformaldehyde (PLP) buffer [0.05 M phosphate buffer, 0.1 M L-lysine (Sigma-Aldrich), 2 mg/mL $NaIO_4$ (ThermoFisher Scientific), 4%

paraformaldehyde; pH 7.4]. Dehydration, delipidation, and clarification of lungs were performed at 37°C under slight agitation (100 rpm) before multiphoton microscopy as previously described (Jing et al. 2018). Briefly, lungs were delipidated by making successive baths of tert-butanol + 3% Quadrol (30%, 50%, and 70% for 2, 4, and 4 h respectively). Following this step, a dehydration step was carried out by incubation in 70% tert-butanol-30% PEG for 24 h. Finally, for clarification, incubation in a 75% benzyl-benzoate–25% PEG solution for 12 h was performed. All products were purchased from Sigma-Aldrich. Cleared lungs were maintained between a slide and a cover-slide in a 2.5 mm thick imaging chamber (CoverWell; Thermo Fischer Scientific) filled with ethylcinnamate (Sigma). Multiphoton microscopy for 3D cleared lung was performed using a Leica Dive upright multiphoton microscope equipped with a 25x/1.0 objective and a Ti-Sapphire femtosecond laser, Chameleon-Ultra II (Coherent Inc.). Second harmonic generation of collagen/bacteries and Siglec1-mGFP emission signals were detected at 920 nm thanks to the respective bandpass filters: blue (430-485 nm), and green (512–551 nm), and mTomato signal was detected at 870 nm thank to 580-623 nm band pass filter. Images were analyzed using Imaris 7.6.1 software (Bitplane).

Three-dimensional segmentation and analysis of TB lesion in cleared lungs

The segmentations were performed using Fiji/ImageJ plugins and tools. Granulomas, blood vessels, and bronchi were segmented from channel C2. Granulomas were segmented using the Labkit plugin. Pre-processing of granulomas involved applying a median filter and despeckling. Post-processing was then applied to remove irrelevant, isolated ROIs. The blood vessels (identified by their red blood cell content) and bronchi were manually segmented using the polygon and magic wand tools, respectively.

Statistical analysis

Sample sizes (n), statistical tests, and significance thresholds are indicated in the figure legends. Analyses were performed in Prism 10.0 (GraphPad). Depending on the experiment, one-way ANOVA or unpaired two-tailed Student's t-test was used as specified in the legends. Significance thresholds were $p < 0.05$ (*), $p < 0.005$ (**), $p < 0.0005$ (***), and $p < 0.0001$ (****).

Declarations

Authorship Contributions

L.F. conducted experiments, analysed data and drafted the manuscript. A.-I.A.-H. performed experiments and analyses. E.B. performed lung clearing and segmentation analyses. Z.P.H contributed to generation and use of C7-Nur77GFP cells. S.Mo. contributed to the generation of Siglec1-mTmG mice and funding of lung intravital imaging set up in BSL3. J.-P.G. provided financial support and scientific guidance. E.M. provided financial support and supervised L.F. throughout the project. D.H, O.N. and J.D.E. secured major funding and provided regular, in-depth scientific guidance, contributing to experimental design and key expertise in immunity and mouse models of tuberculosis. S.Ma. designed and built the surgical platform and lung window, coded all in-house Python scripts for cell tracking and behaviour analysis, and

performed image and movie analyses. E.L. supervised the project, designed, performed and analysed experiments, and wrote the manuscript. All authors critically revised the manuscript.

Acknowledgments

We acknowledge the cytometry (Genotoul TRI-IPBS) and animal (Genotoul Anexplo-IPBS) facilities, particularly Flavie Moreau, Malory Blasco and Celine Berrone for technical support. TRI-IPBS is member of the national infrastructure France-BioImaging (https://ror.org/01y7vt929) supported by the French National Research Agency (ANR-24-INBS-0005 FBI BIOGEN); Anexplo-IPBS is member of the national infrastructure Celphedia (https://ror.org/00v2cdz24). This work was supported by Fonds de Recherche en Santé Respiratoire - Fondation du Souffle (Grant #198942 to E.L), ANRS (PhD fellowship to L.F), University of Toulouse (Tremplin 2022 #0003970), National Institute of Health NIH (R21 to EL, D.H, ON, and JE), and Horizon Europe TBVAC-Horizon (Grant #101080309 to D.H, O.N and E.L). Figures were created with Biorender.com.

References

1. Ariyachaokun, Kanchiyaphat, Anna D. Grabowska, Claude Gutierrez, et Olivier Neyrolles. 2020. « Multi-Stress Induction of the Mycobacterium Tuberculosis MbcTA Bactericidal Toxin-Antitoxin System ». *Toxins* 12 (5): 329. https://doi.org/10.3390/toxins12050329.
2. Bajénoff, Marc, Jackson G. Egen, Lily Y. Koo, et al. 2006. « Stromal Cell Networks Regulate Lymphocyte Entry, Migration, and Territoriality in Lymph Nodes ». *Immunity* 25 (6): 989-1001. https://doi.org/10.1016/j.immuni.2006.10.011.
3. Barlerin, D., G. Bessière, J. Domingues, M. Schuette, C. Feuillet, et A. Peixoto. 2017. « Biosafety Level 3 Setup for Multiphoton Microscopy in Vivo ». *Scientific Reports* 7 (1): 571. https://doi.org/10.1038/s41598-017-00702-x.
4. Boldajipour, Bijan, Amanda Nelson, et Matthew F. Krummel. 2016. « Tumor-Infiltrating Lymphocytes Are Dynamically Desensitized to Antigen but Are Maintained by Homeostatic Cytokine ». *JCI Insight* 1 (20): e89289. https://doi.org/10.1172/jci.insight.89289.
5. Boulch, Morgane, Capucine L. Grandjean, Marine Cazaux, et Philippe Bousso. 2019. « Tumor Immunosurveillance and Immunotherapies: A Fresh Look from Intravital Imaging ». *Trends in Immunology* 40 (11): 1022-34. https://doi.org/10.1016/j.it.2019.09.002.
6. Bromley, S. K., D. A. Peterson, M. D. Gunn, et M. L. Dustin. 2000. « Cutting Edge: Hierarchy of Chemokine Receptor and TCR Signals Regulating T Cell Migration and Proliferation ». *Journal of Immunology (Baltimore, Md.: 1950)* 165 (1): 15-19. https://doi.org/10.4049/jimmunol.165.1.15.
7. Celli, Susanna, Fabrice Lemaître, et Philippe Bousso. 2007. « Real-Time Manipulation of T Cell-Dendritic Cell Interactions in Vivo Reveals the Importance of Prolonged Contacts for CD4+ T Cell Activation ». *Immunity* 27 (4): 625-34. https://doi.org/10.1016/j.immuni.2007.08.018.
8. Cohen, Sara B., Benjamin H. Gern, et Kevin B. Urdahl. 2022. « The Tuberculous Granuloma and Preexisting Immunity ». *Annual Review of Immunology* 40 (avril): 589-614.

https://doi.org/10.1146/annurev-immunol-093019-125148.

9. Datta, Meenal, Laura E. Via, Walid S. Kamoun, et al. 2015. « Anti-Vascular Endothelial Growth Factor Treatment Normalizes Tuberculosis Granuloma Vasculature and Improves Small Molecule Delivery ». *Proceedings of the National Academy of Sciences of the United States of America* 112 (6): 1827-32. https://doi.org/10.1073/pnas.1424563112.
10. Egen, Jackson G., Antonio Gigliotti Rothfuchs, Carl G. Feng, Marcus A. Horwitz, Alan Sher, et Ronald N. Germain. 2011. « Intravital Imaging Reveals Limited Antigen Presentation and T Cell Effector Function in Mycobacterial Granulomas ». *Immunity* 34 (5): 807-19. https://doi.org/10.1016/j.immuni.2011.03.022.
11. Egen, Jackson G., Antonio Gigliotti Rothfuchs, Carl G. Feng, Nathalie Winter, Alan Sher, et Ronald N. Germain. 2008. « Macrophage and T Cell Dynamics during the Development and Disintegration of Mycobacterial Granulomas ». *Immunity* 28 (2): 271-84. https://doi.org/10.1016/j.immuni.2007.12.010.
12. Flynn, JoAnne L., et John Chan. 2022. « Immune Cell Interactions in Tuberculosis ». *Cell* 185 (25): 4682-702. https://doi.org/10.1016/j.cell.2022.10.025.
13. Gideon, Hannah P., Travis K. Hughes, Constantine N. Tzouanas, et al. 2022. « Multimodal Profiling of Lung Granulomas in Macaques Reveals Cellular Correlates of Tuberculosis Control ». *Immunity* 55 (5): 827-846.e10. https://doi.org/10.1016/j.immuni.2022.04.004.
14. *Global Tuberculosis Report 2025*. 2025. 1st ed. World Health Organization.
15. Gunzer, M., A. Schäfer, S. Borgmann, et al. 2000. « Antigen Presentation in Extracellular Matrix: Interactions of T Cells with Dendritic Cells Are Dynamic, Short Lived, and Sequential ». *Immunity* 13 (3): 323-32. https://doi.org/10.1016/s1074-7613(00)00032-7.
16. Headley, Mark B., Adriaan Bins, Alyssa Nip, et al. 2016. « Visualization of Immediate Immune Responses to Pioneer Metastatic Cells in the Lung ». *Nature* 531 (7595): 513-17. https://doi.org/10.1038/nature16985.
17. Hor, Jyh Liang, et Ronald N. Germain. 2022. « Intravital and High-Content Multiplex Imaging of the Immune System ». *Trends in Cell Biology* 32 (5): 406-20. https://doi.org/10.1016/j.tcb.2021.11.007.
18. Jasenosky, Luke D., Thomas J. Scriba, Willem A. Hanekom, et Anne E. Goldfeld. 2015. « T Cells and Adaptive Immunity to Mycobacterium Tuberculosis in Humans ». *Immunological Reviews* 264 (1): 74-87. https://doi.org/10.1111/imr.12274.
19. Ji, Daisy X., Kristen C. Witt, Dmitri I. Kotov, et al. 2021. « Role of the Transcriptional Regulator SP140 in Resistance to Bacterial Infections via Repression of Type I Interferons ». *eLife* 10 (juin): e67290. https://doi.org/10.7554/eLife.67290.
20. Jing, Dian, Shiwen Zhang, Wenjing Luo, et al. 2018. « Tissue Clearing of Both Hard and Soft Tissue Organs with the PEGASOS Method ». *Cell Research* 28 (8): 803-18. https://doi.org/10.1038/s41422-018-0049-z.
21. Kauffman, K. D., M. A. Sallin, S. Sakai, et al. 2018. « Defective Positioning in Granulomas but Not Lung-Homing Limits CD4 T-Cell Interactions with Mycobacterium Tuberculosis-Infected

Macrophages in Rhesus Macaques ». *Mucosal Immunology* 11 (2): 462-73. https://doi.org/10.1038/mi.2017.60.

22. Kerdidani, Dimitra, Emmanouil Aerakis, Kleio-Maria Verrou, et al. 2022. « Lung Tumor MHCII Immunity Depends on in Situ Antigen Presentation by Fibroblasts ». *The Journal of Experimental Medicine* 219 (2): e20210815. https://doi.org/10.1084/jem.20210815.
23. Lefrançais, Emma, Denis Hudrisier, Olivier Neyrolles, Samuel M. Behar, et Joel D. Ernst. 2025. « Finding and Filling the Knowledge Gaps in Mechanisms of T Cell-Mediated TB Immunity to Inform Vaccine Design ». *Nature Reviews. Immunology*, publication en ligne anticipée, juin 13. https://doi.org/10.1038/s41577-025-01192-z.
24. Looney, Mark R., et Mark B. Headley. 2020. « Live Imaging of the Pulmonary Immune Environment ». *Cellular Immunology* 350 (avril): 103862. https://doi.org/10.1016/j.cellimm.2018.09.007.
25. Looney, Mark R, Emily E Thornton, Debasish Sen, Wayne J Lamm, Robb W Glenny, et Matthew F Krummel. 2011. « Stabilized Imaging of Immune Surveillance in the Mouse Lung ». *Nature Methods* 8 (1): 91-96. https://doi.org/10.1038/nmeth.1543.
26. McCaffrey, Erin F., Michele Donato, Leeat Keren, et al. 2022. « The Immunoregulatory Landscape of Human Tuberculosis Granulomas ». *Nature Immunology* 23 (2): 318-29. https://doi.org/10.1038/s41590-021-01121-x.
27. Moreau, Hélène D., Fabrice Lemaître, Kym R. Garrod, Zacarias Garcia, Ana-Maria Lennon-Duménil, et Philippe Bousso. 2015. « Signal Strength Regulates Antigen-Mediated T-Cell Deceleration by Distinct Mechanisms to Promote Local Exploration or Arrest ». *Proceedings of the National Academy of Sciences of the United States of America* 112 (39): 12151-56. https://doi.org/10.1073/pnas.1506654112.
28. Mrass, Paulus, Sreenivasa Rao Oruganti, G. Matthew Fricke, et al. 2017. « ROCK Regulates the Intermittent Mode of Interstitial T Cell Migration in Inflamed Lungs ». *Nature Communications* 8 (1): 1010. https://doi.org/10.1038/s41467-017-01032-2.
29. Oehlers, Stefan H., Mark R. Cronan, Ninecia R. Scott, et al. 2015. « Interception of Host Angiogenic Signalling Limits Mycobacterial Growth ». *Nature* 517 (7536): 612-15. https://doi.org/10.1038/nature13967.
30. Onder, Lucas, Chrysa Papadopoulou, Almut Lütge, et al. 2025. « Fibroblastic Reticular Cells Generate Protective Intratumoral T Cell Environments in Lung Cancer ». *Cell* 188 (2): 430-446.e20. https://doi.org/10.1016/j.cell.2024.10.042.
31. Overstreet, Michael G, Alison Gaylo, Bastian R Angermann, et al. 2013. « Inflammation-Induced Interstitial Migration of Effector CD4+ T Cells Is Dependent on Integrin αV ». *Nature Immunology* 14 (9): 949-58. https://doi.org/10.1038/ni.2682.
32. Pittet, Mikael J., Christopher S. Garris, Sean P. Arlauckas, et Ralph Weissleder. 2018. « Recording the Wild Lives of Immune Cells ». *Science Immunology* 3 (27): eaaq0491. https://doi.org/10.1126/sciimmunol.aaq0491.

33. Ray, Steven J., Suzanne N. Franki, Robert H. Pierce, et al. 2004. « The Collagen Binding Alpha1beta1 Integrin VLA-1 Regulates CD8 T Cell-Mediated Immune Protection against Heterologous Influenza Infection ». *Immunity* 20 (2): 167-79. https://doi.org/10.1016/s1074-7613(04)00021-4.
34. Salmon, Hélène, Katarzyna Franciszkiewicz, Diane Damotte, et al. 2012. « Matrix Architecture Defines the Preferential Localization and Migration of T Cells into the Stroma of Human Lung Tumors ». *The Journal of Clinical Investigation* 122 (3): 899-910. https://doi.org/10.1172/JCI45817.
35. Santiago-Carvalho, Igor, Gislane Almeida-Santos, Bruna Gois Macedo, et al. 2023. « T Cell-Specific P2RX7 Favors Lung Parenchymal CD4+ T Cell Accumulation in Response to Severe Lung Infections ». *Cell Reports* 42 (11): 113448. https://doi.org/10.1016/j.celrep.2023.113448.
36. Sawyer, Andrew J., Ellis Patrick, Jarem Edwards, et al. 2023. « Spatial Mapping Reveals Granuloma Diversity and Histopathological Superstructure in Human Tuberculosis ». *The Journal of Experimental Medicine* 220 (6): e20221392. https://doi.org/10.1084/jem.20221392.
37. Srivastava, Smita, et Joel D. Ernst. 2013. « Cutting Edge: Direct Recognition of Infected Cells by CD4 T Cells Is Required for Control of Intracellular Mycobacterium Tuberculosis in Vivo ». *Journal of Immunology (Baltimore, Md.: 1950)* 191 (3): 1016-20. https://doi.org/10.4049/jimmunol.1301236.
38. Sumen, Cenk, Thorsten R. Mempel, Irina B. Mazo, et Ulrich H. von Andrian. 2004. « Intravital Microscopy: Visualizing Immunity in Context ». *Immunity* 21 (3): 315-29. https://doi.org/10.1016/j.immuni.2004.08.006.
39. Topham, D. J., M. R. Castrucci, F. S. Wingo, G. T. Belz, et P. C. Doherty. 2001. « The Role of Antigen in the Localization of Naive, Acutely Activated, and Memory CD8(+) T Cells to the Lung during Influenza Pneumonia ». *Journal of Immunology (Baltimore, Md.: 1950)* 167 (12): 6983-90. https://doi.org/10.4049/jimmunol.167.12.6983.
40. Wells, Gordon, Joel N. Glasgow, Kievershen Nargan, et al. 2021. « Micro-Computed Tomography Analysis of the Human Tuberculous Lung Reveals Remarkable Heterogeneity in Three-Dimensional Granuloma Morphology ». *American Journal of Respiratory and Critical Care Medicine* 204 (5): 583-95. https://doi.org/10.1164/rccm.202101-0032OC.
41. Wilson, Emma H., Tajie H. Harris, Paulus Mrass, et al. 2009. « Behavior of Parasite-Specific Effector CD8+ T Cells in the Brain and Visualization of a Kinesis-Associated System of Reticular Fibers ». *Immunity* 30 (2): 300-311. https://doi.org/10.1016/j.immuni.2008.12.013.
42. You, Ran, Jordan Artichoker, Adam Fries, et al. 2021. « Active Surveillance Characterizes Human Intratumoral T Cell Exhaustion ». *The Journal of Clinical Investigation* 131 (18): e144353. https://doi.org/10.1172/JCI144353.

Figures

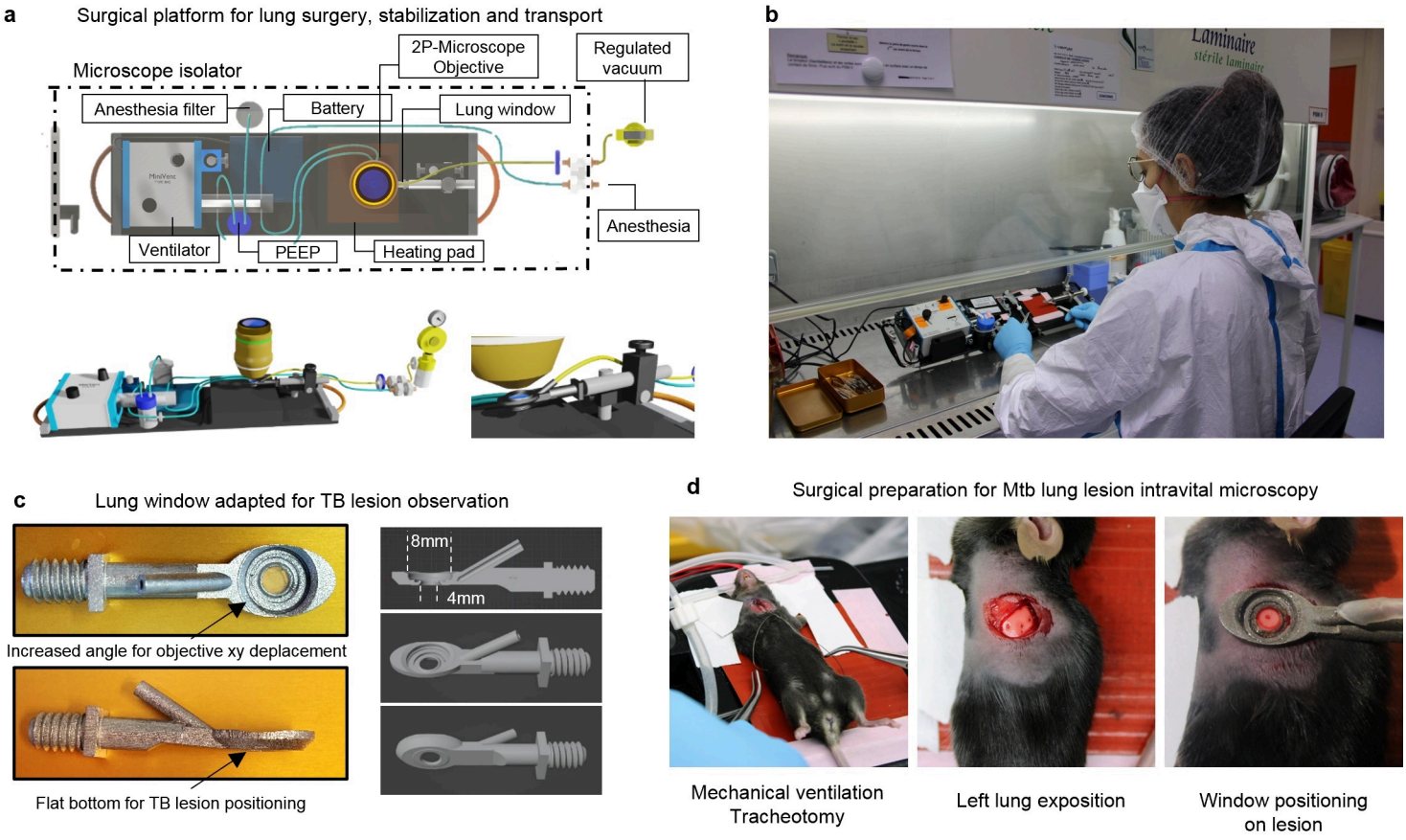

Figure 1

Intravital microscopy platform for real-time imaging of *Mycobacterium tuberculosis*–infected lungs under BSL-3 conditions.

a, Custom-designed platform allowing lung stabilization and secure transfer of anesthetized, ventilated mice from the biosafety cabinet to the microscope isolator. **b,**Surgical setup in the BSL-3 cabinet using the custom platform. **c,**Modified lung imaging window optimized for visualization of tuberculosis lesions (adapted from Headley *et al.*, *Nature* 2016). **d,**Surgical preparation for lung intravital microscopy (LIVM), including tracheotomy for mechanical ventilation, thoracotomy exposing the left lung with visible lesions, and stabilization with a custom suction imaging window.

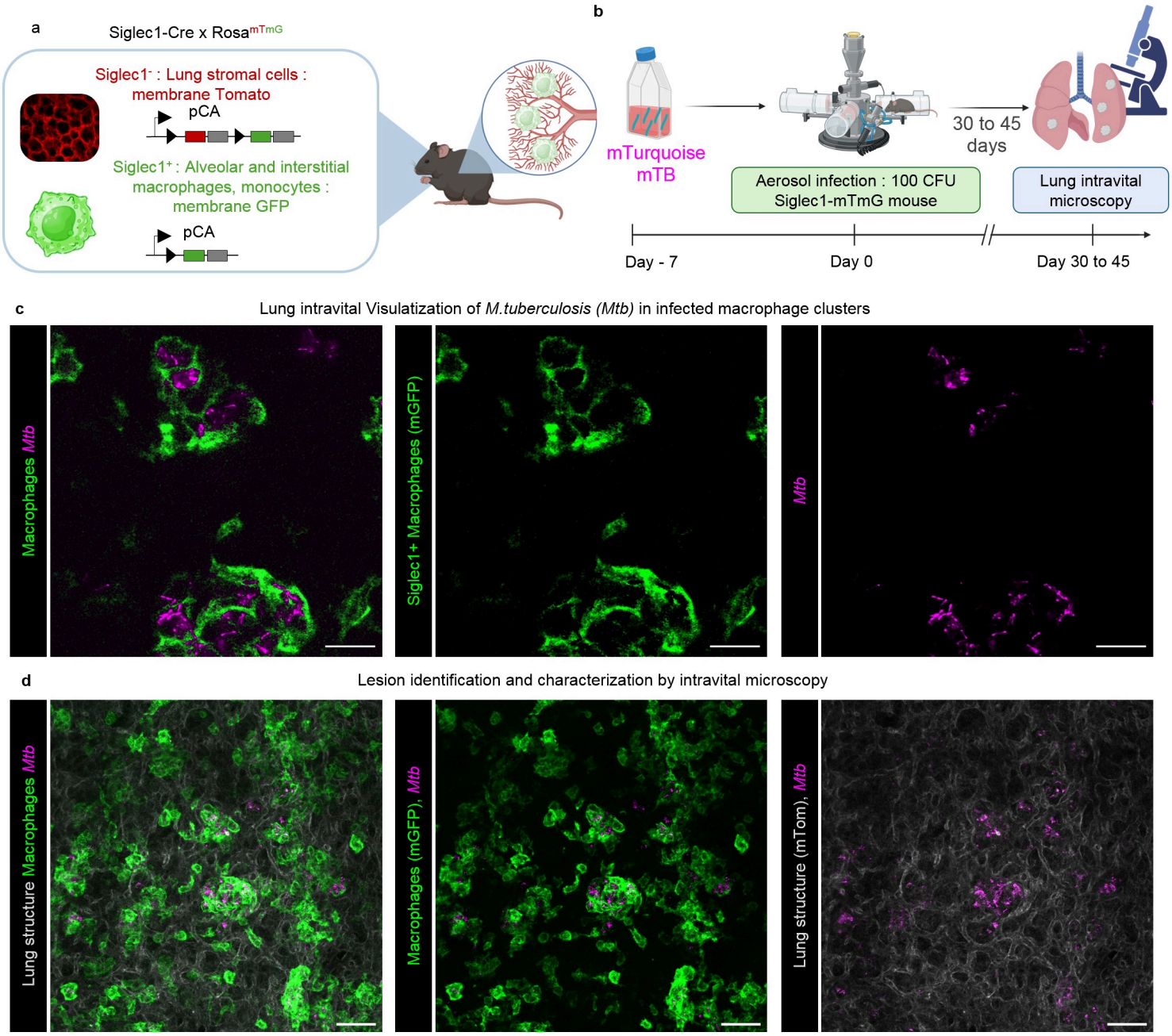

Figure 2

Real time visualization of *M. tuberculosis* within infected macrophage clusters.

a, Schematic of macrophage reporter mice. **b,** Infection protocol for lung intravital microscopy (LIVM). **c-d,** LIVM images showing *M. tuberculosis*(magenta) as single bacteria within Siglec1⁺ macrophage clusters (membrane GFP) in infected lungs. **d,** Identification and characterization of TB lesions by intravital microscopy.

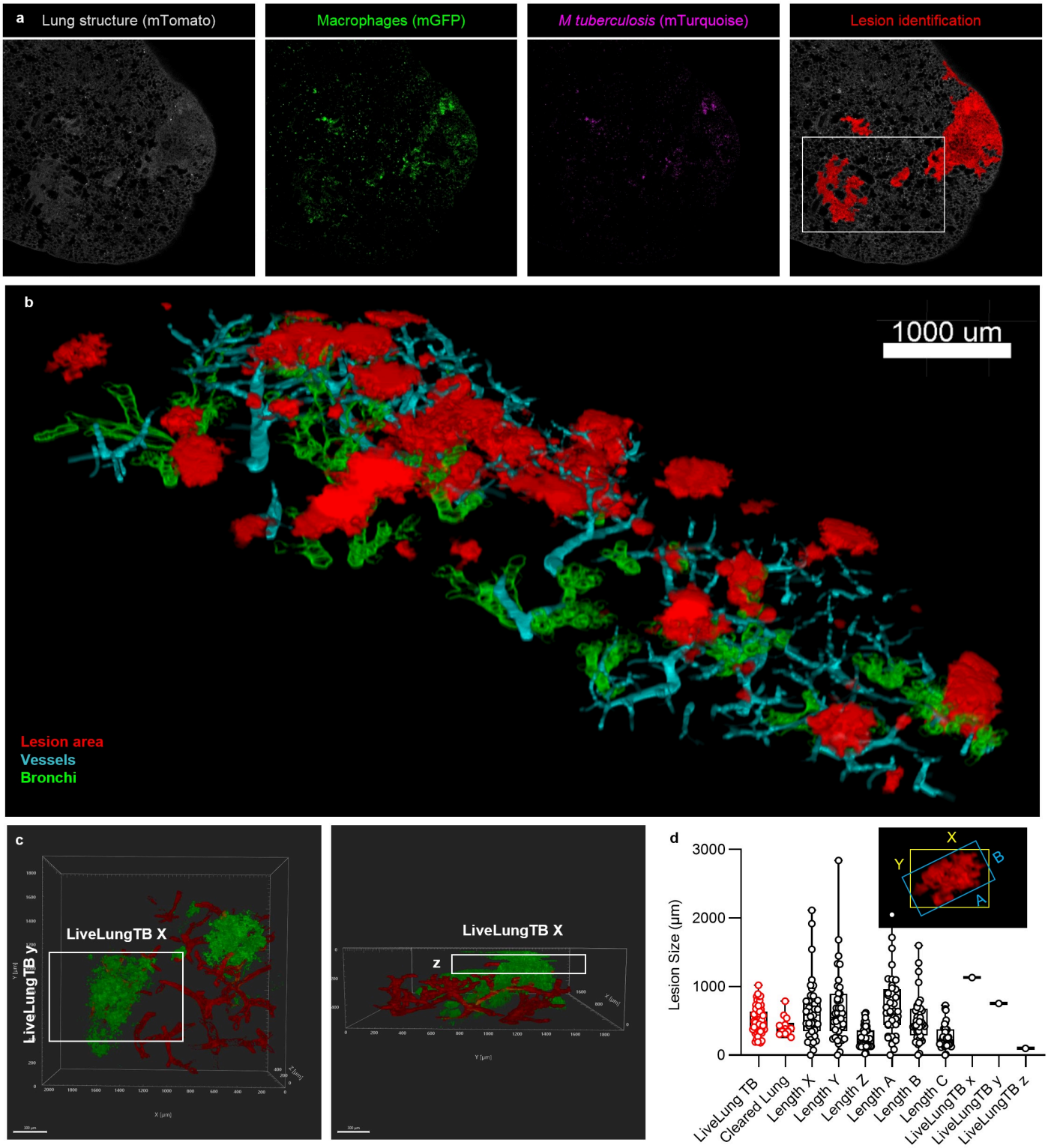

Figure 3

3D clearing and characterization of lung TB lesions and intravital imaging field. a,Whole-lung lobe clearing and 3D segmentation of lesions. Colors: grey, lung structure (mTomato); green, Siglec1$^+$ macrophage membranes (mGFP); magenta, M. tuberculosis (mturquoise), red, segmented lesions **b,** 3D reconstruction showing lesions (red), large vessels (blue), and bronchi (green) in infected cleared lung. **c,** Representation of intravital imaging field (white rectangle; 3 × 2 tiles, 1,134 × 756 × 100 µm) illustrating

that the LIVM observation area covers an entire lesion in X and Y dimensions but not along the full Z-axis. **d,** Representation of lesion size heterogeneity, including the equivalent diameter of lesions detected by intravital microscopy or in the cleared whole lobe (in red), as well as the X, Y, Z dimensions (bounding box X,Y,Z, A, B, C) measured in the cleared lobe, compared with the corresponding LIVM observation volume dimension (LiveLung-TB X, Y, Z).

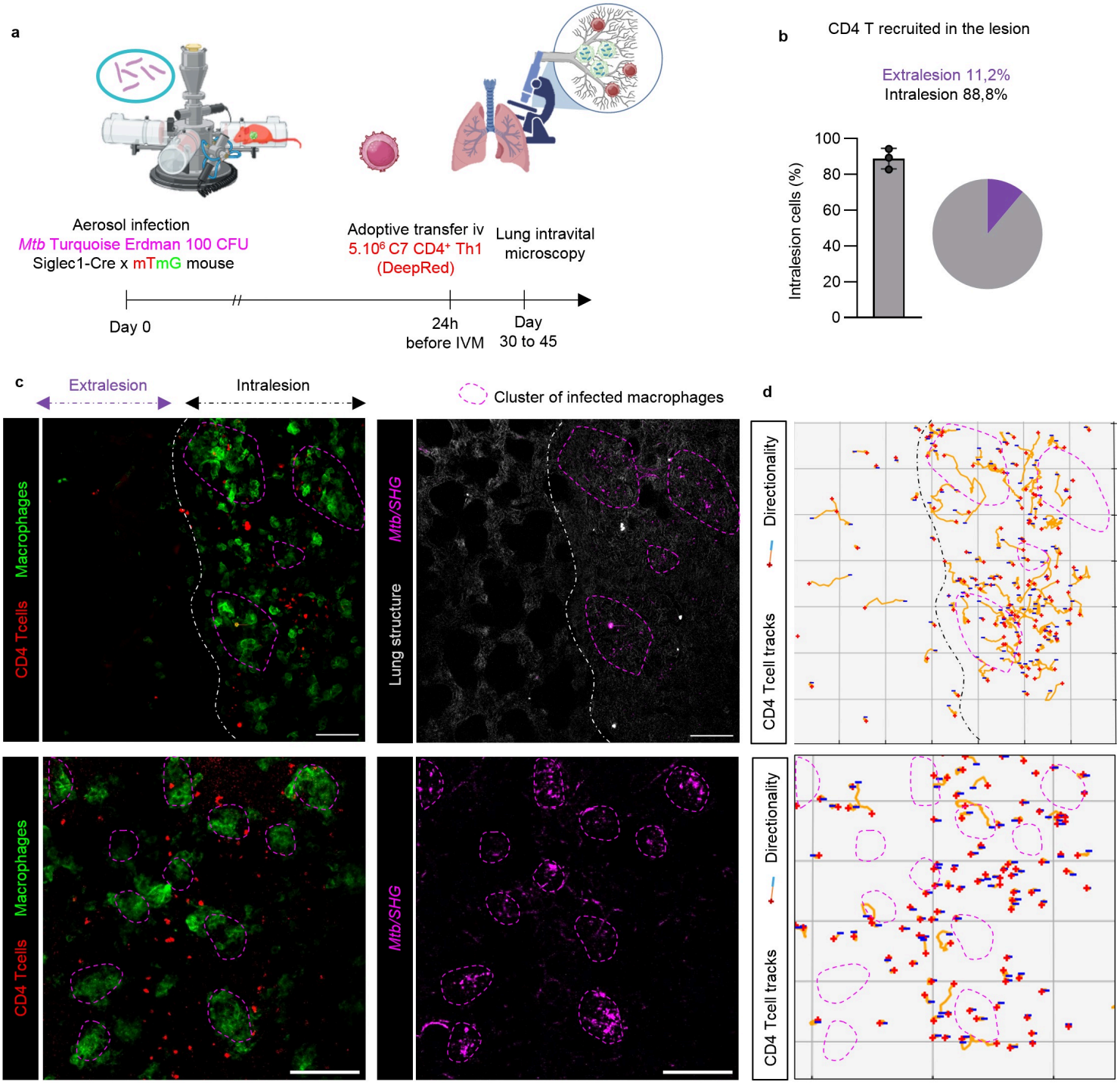

Figure 4

CD4⁺ T cells infiltrate TB lesions and accumulate around clusters of infected macrophages.

a, Schematic of C7 CD4⁺ T cell adoptive transfer into *Mycobacterium tuberculosis*–infected mice prior to lung intravital microscopy (LIVM). **b,** Quantification of CD4⁺ T cell localization, expressed as the percentage of tracks inside versus outside lesions (intralesional vs. extralesional). Mean data from three infected mice (n = 3), representing 169, 282, and 460 total CD4⁺ T cell tracks **c,**Representative LIVM images showing CD4⁺ T cell distribution relative to TB lesions (white dashed lines) and clusters of infected macrophages (purple dashed circles). Scale bar, 100µm **d,** Corresponding spatial maps of tracked CD4⁺ T cells overlaid on lesion and macrophage cluster locations.

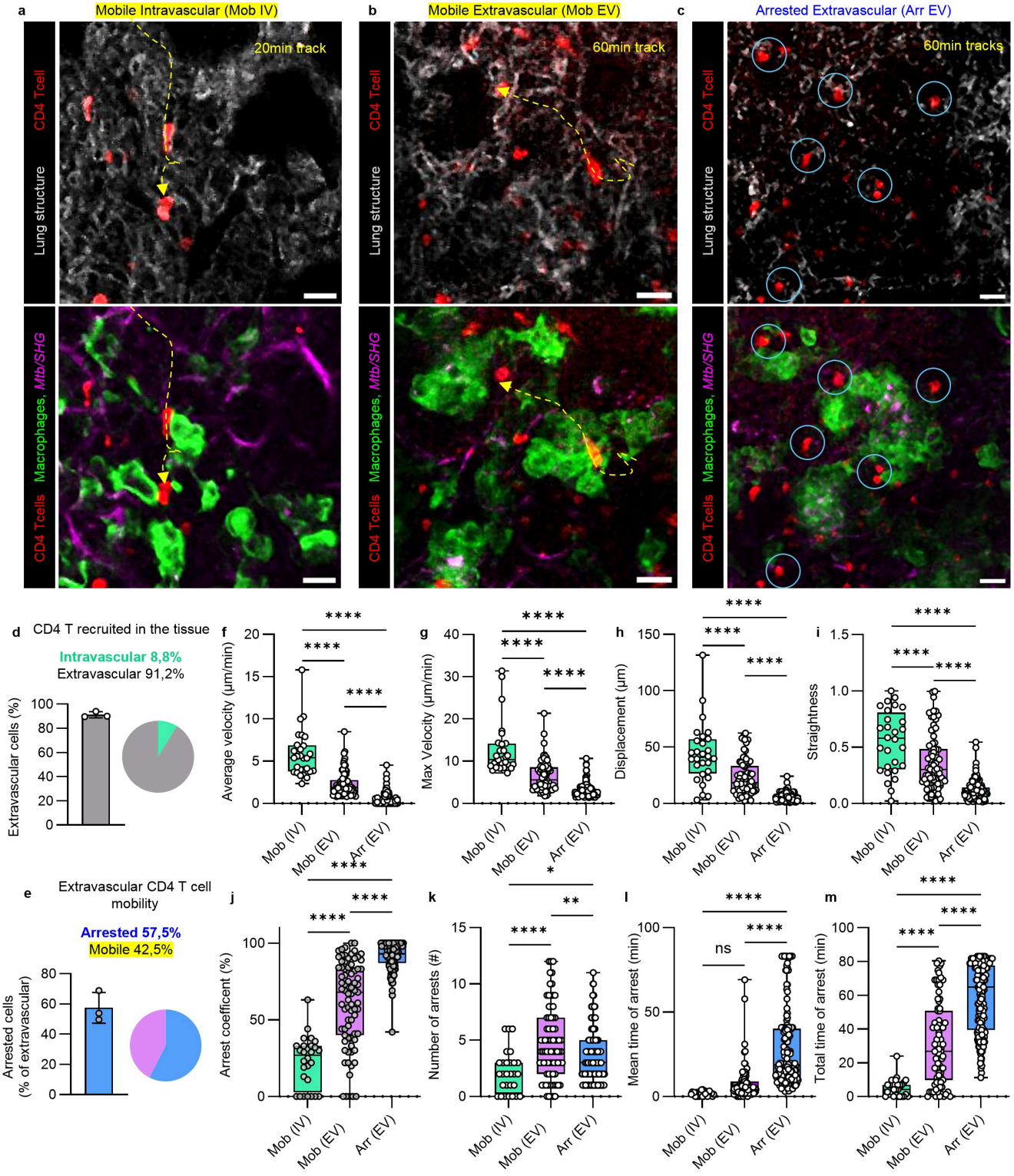

Figure 5

Intravital imaging reveals CD4⁺ T cell migratory states in Mtb infection

a-c, Representative LIVM images showing mobile intravascular **a**, mobile extravascular **b**, and arrested extravascular **c,** C7 CD4⁺ T cells. Scale bar, 20 μm. **d,**Proportion of intravascular and extravascular cells among all tracked cells. **e,**Proportion of arrested versus mobile cells within the extravascular compartment. **f-i,** Quantification of behavioral parameters: average velocity, maximum velocity, displacement, and straightness, for the three identified populations. **j,** Arrest coefficient, expressed as the percentage of time each cell exhibited an instant speed <2 μm/min. **k-m,**Number of arrests, mean duration of arrest, and total time arrested per track. **d–e:** Mean data from three infected mice (n = 3). **f–i** and **j–m**: Behavioral parameters were extracted from all tracks within a single video and classified as mobile intravascular (Mob IV), mobile extravascular (Mob EV), or arrested extravascular (Arr EV), with 28, 79, and 254 tracks, respectively.

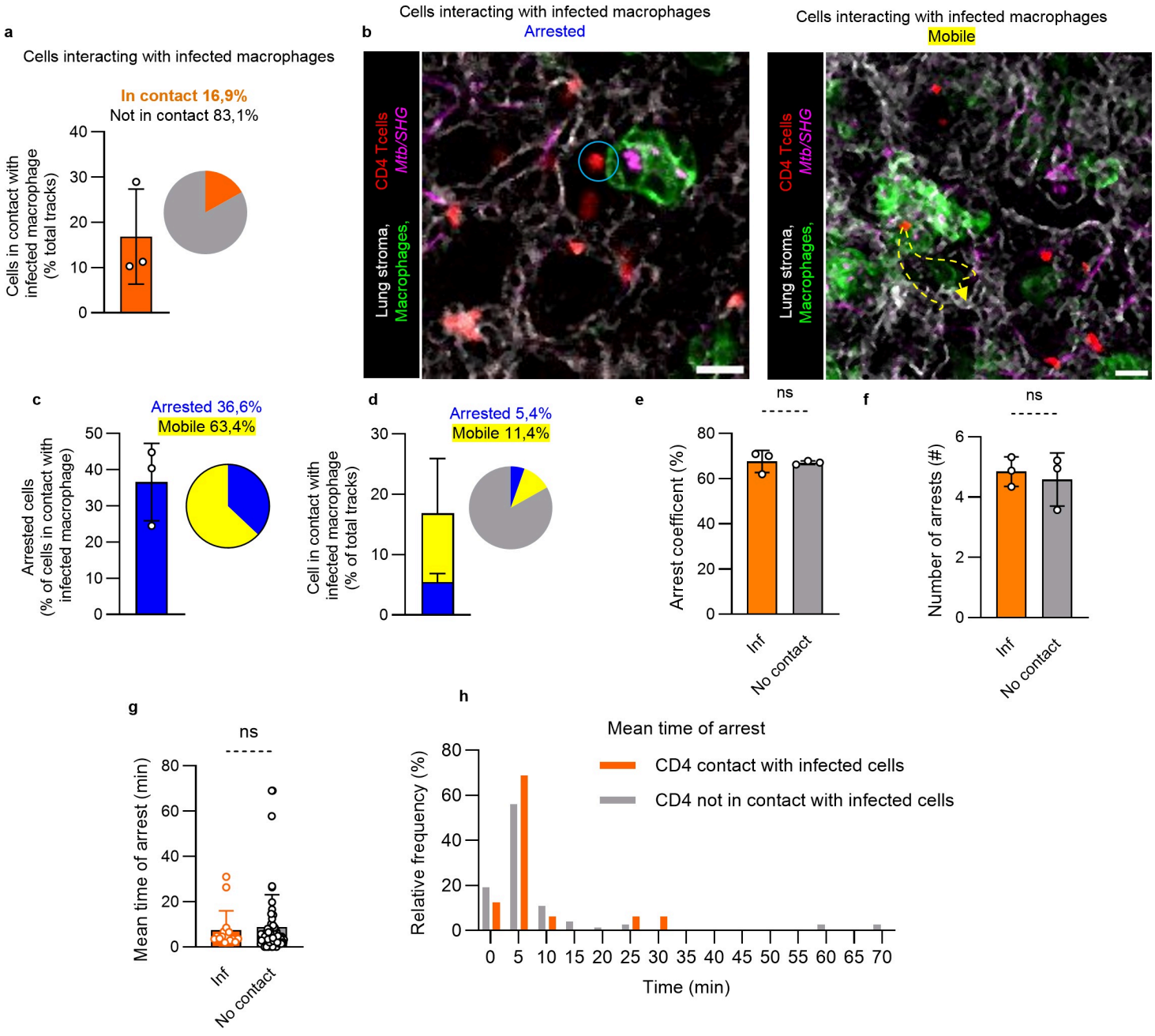

Figure 6

CD4⁺ T cell contacts with infected macrophages are rare and transient.

a, Fraction of tracked CD4⁺ T cells establishing contacts with infected macrophages (% of total tracks). **b,** Representative intravital microscopy images showing CD4⁺ T cells interacting with *Mycobacterium tuberculosis*–infected macrophages, either arrested or mobile. Scale bar, 20 µm. **c,** Proportion of T cells arrested while in contact with infected macrophages (% of contacting cells). **d,** Overall proportion of arrested T cells relative to the total tracked population (% of total tracks). **e,**Arrest coefficient (expressed as the percentage of time a cell remains arrested per track), **f,** number of arrest events, and **g-h,** Mean arrest duration of motile T cells transiently engaging infected macrophages, compared with T cells that do not contact infected cells; shown in **g** as a bar graph (mean ± SD) and in **h** as a frequency histogram

(n = 16 and 73 tracks, respectively, from one mouse) **a, c-f** Mean data from three infected mice (n = 3), representing 169, 282, and 460 total tracks, respectively.

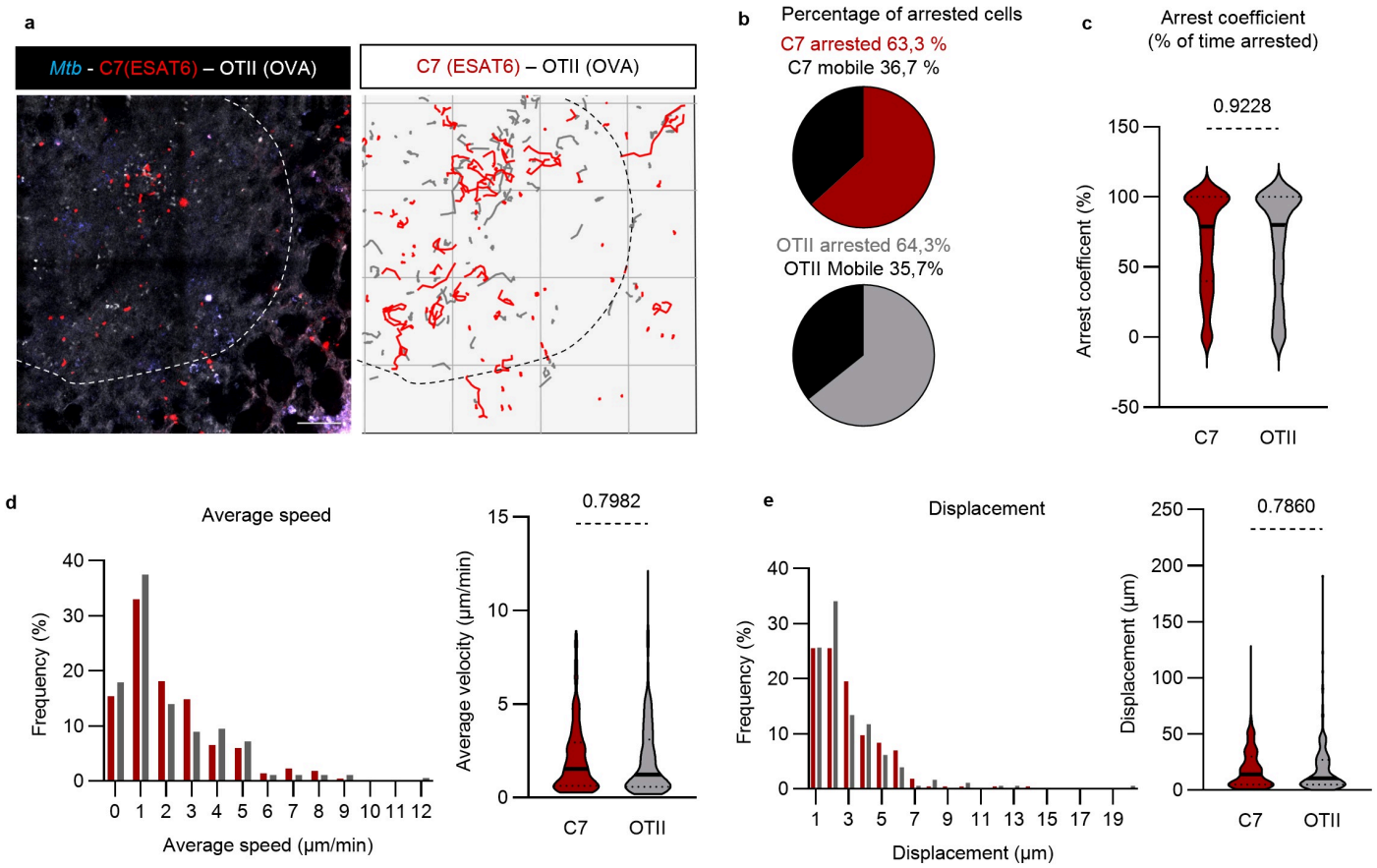

Figure 7

T cell arrest is not dependent on antigen recognition.

a, Representative intravital images and migration tracks of C7 (M. tuberculosis-specific) and OT-II (non-specific) CD4⁺ T cells in infected lungs, observed by LIVM. Scale bar, 100µm. comparison of motility parameters between antigen-specific and non-specific T cells. **b,**Percentage of arrested cells. **c,** Arrest coefficient (percentage of time each cell spent arrested). **d,** Average speed **e,** Displacement. Data are displayed as violin plots, showing the full distribution of values with kernel density estimation; the median is indicated by a central line and dashed lines mark the quartiles. n= 215 C7 and 179 OTII tracks collected from one mouse, representative of three independent mice.

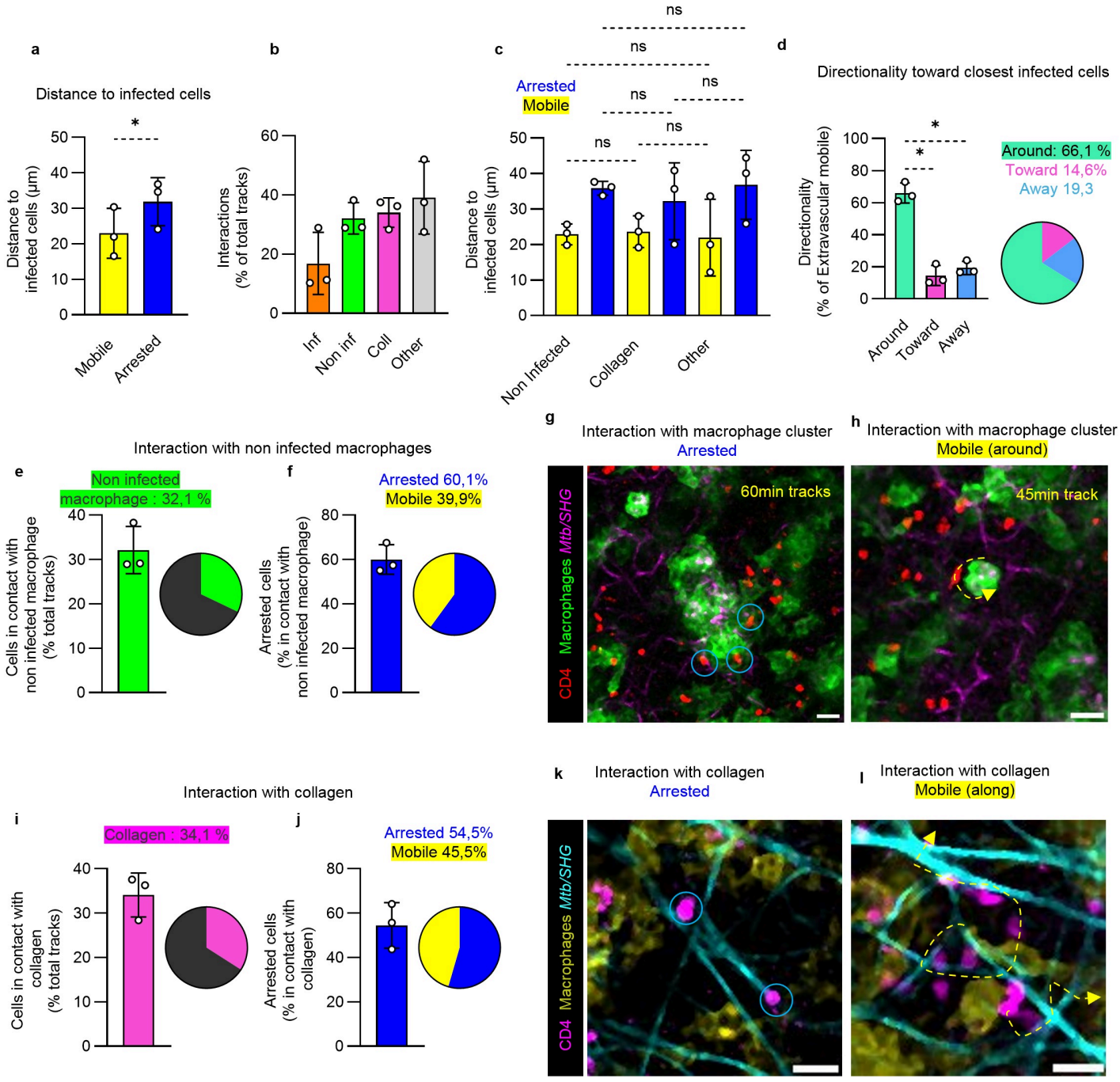

Figure 8

CD4⁺ T cell migration and arrest are influenced by macrophage clusters and collagen fibers.

a, Distance to the nearest infected cell for mobile and arrested extravascular CD4⁺ T cells. **b,**Proportion of extravascular T cells interacting with infected macrophages, uninfected macrophage, collagen fibers, or other structures (% of total tracks). **c,** Distance to the nearest infected cell for mobile and arrested extravascular T cells, categorized by interaction type (uninfected macrophage, collagen fibers, or other). **d,** Directionality of mobile extravascular T cells relative to the nearest infected macrophage, expressed as the percentage of cells moving toward, around, or away from the target. **e,**Proportion of T cells

interacting with uninfected macrophage, and **f,**percentage of these cells that are arrested or mobile. **g,h,**Representative intravital lung images showing a $CD4^+$ T cell **g**, arrested on or h, migrating around a macrophage cluster. **i,** Proportion of T cells interacting with collagen fibers and **j,** percentage of these cells that are arrested or mobile. Scale bar, 20μm **k,l,** Representative intravital lung images showing a $CD4^+$ T cell **k,** arrested on a collagen fiber (second harmonic generation, SHG) or **l,** migrating along a collagen fiber. Mean data from three infected mice (n = 3) representing 169, 282, and 460 total tracks, respectively

Supplementary Files

This is a list of supplementary files associated with this preprint. Click to download.

- ExtendedDataFigure1.jpg
- ExtendedDataFigure2.jpg
- ExtendedDataFigure3.jpg
- ExtendedDataFigure4.jpg
- ExtendedDataFigure5.jpg
- ExtendedDataFigure6.jpg
- SupplementaryVideo1.mp4
- SupplementaryVideo2.mp4
- SupplementaryVideo3.mp4
- SupplementaryVideo4.mp4
- SupplementaryVideo5.mp4
- SupplementaryVideo6.mp4
- SupplementaryVideo7.mp4